Chapter 10
Measuring Atomic Magnetic Moments in Magnetic Nanostructures Using X-Ray Magnetic Circular Dichroism (XMCD)

Chris Binns, José Angel de Toro, and Peter Normile

Abstract The chapter describes the development of X-ray magnetic circular dichroism (XMCD) using circularly polarised soft X-ray photons from synchrotron sources. Following the derivation of X-ray absorption sum rules for magnetic materials, the technique became a powerful probe of magnetism able to separately measure the atomic and spin orbital magnetic moments independently for each magnetic element in the sample. The majority of the experiments have focused on the L-absorption edges of transition metals and the method has been particularly useful in identifying the source of enhanced magnetic moments in nanostructures. The chapter illustrates the power of the method with a specific example, that of Fe@Cr core–shell nanoparticles with different Cr shell thicknesses. Here, it was shown that at least two Cr atomic layers are required to see the onset of the exchange bias effect at the ferromagnetic–antiferromagnetic interface. The future perspectives of the technique are described including spatially resolved XMCD and time-resolved XMCD measurements.

10.1 Introduction

X-ray magnetic circular dichroism (XMCD) has emerged as a powerful tool that is capable of measuring element-specific atomic orbital and spin magnetic moments in materials. The technique has enabled some important breakthroughs in the understanding of the magnetic behaviour of nanostructures. Magnetic circular dichroism in the UV band has been known since the nineteenth century but X-ray magnetic circular dichroism began to be of interest as a magnetic measurement method in the 1970s. Erskine and Stern predicted in 1975 that circularly polarised X-rays could provide information on the valence band spin polarisation of Ni [1]. In 1987, a measurement of the transmission of synchrotron radiation through thin Fe films showed a difference

C. Binns (✉) · J. A. de Toro · P. Normile
Instituto Regional de Investigación Científica Aplicada (IRICA), Av. Camilo José Cela, 1, 13005 Ciudad Real, Spain
e-mail: christopher.binns@uclm.es

D. Peddis et al. (eds.), *New Trends in Nanoparticle Magnetism*,
Springer Series in Materials Science 308,
https://doi.org/10.1007/978-3-030-60473-8_10

in K-edge absorption for left and right circularly polarised photons [2]. As shown by Erskine and Stern, however, in the case of transition metals, $L_{2,3}$-edge absorption in the soft X-ray band is potentially a more powerful source of information though technically more difficult. An important breakthrough starting in the early 1980s was the emergence of dedicated synchrotron radiation sources that could produce high intensities of circularly polarised soft X-rays.

Figure 10.1 shows the two basic experimental set-ups for the measurement of dichroism in the *L*-edge absorption spectrum of a sample containing a transition metal. The photon beam is circularly polarised with the *L*-vector parallel or antiparallel to the beam and the sample magnetisation, ***M***, can be magnetised to saturation parallel or antiparallel to ***L***. Figure 10.1a shows a measurement where the sample can be deposited onto a substrate that is transparent to soft X-rays, for example, a carbon-coated transmission electron microscope (TEM) grid. In this case, the incident and transmitted beams are measured and the difference between them is the X-ray absorption. Figure 10.1b shows the other set-up when the sample is a bulk material or deposited on a substrate opaque to soft X-rays. In this case, the total secondary electron yield, which within certain assumptions is proportional to the X-ray absorption, is measured and normalised to the incident X-ray intensity. The

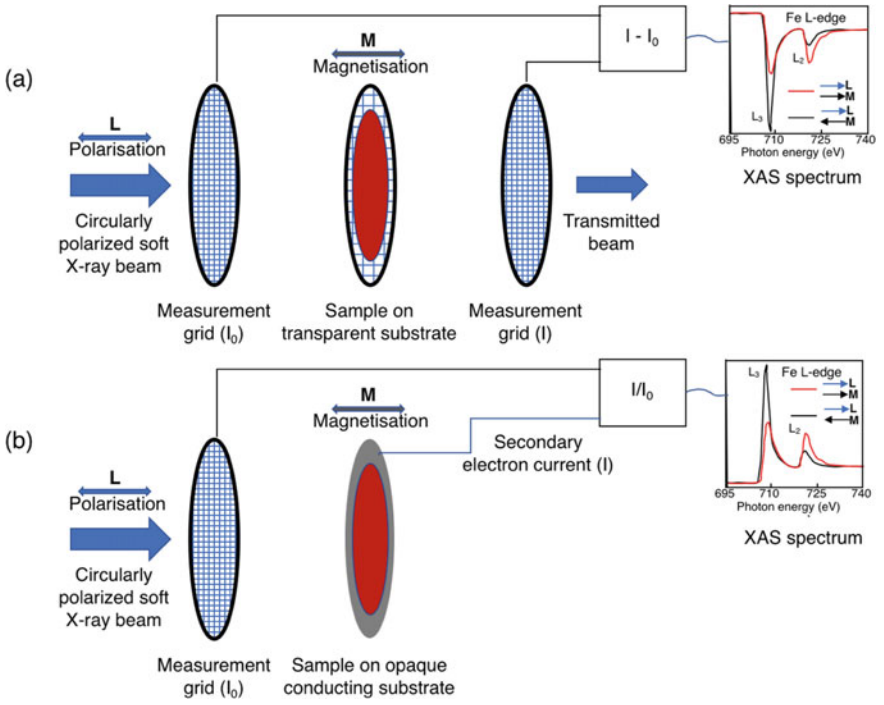

Fig. 10.1 The two basic configurations for measuring XMCD. **a** In transmission for transparent substrates. **b** By using secondary electron yield for opaque and conducting substrates or bulk samples. The example spectra shown are the *L*-edge absorption in samples containing Fe

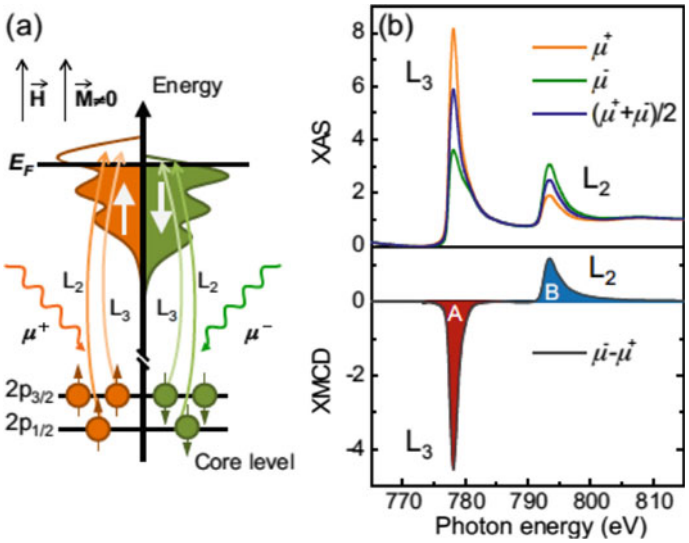

Fig. 10.2 The basic two-step process used to explain *L*-edge X-ray dichroism in a magnetic sample. Positive helicity μ^+ X-ray photons ($\boldsymbol{L} = +1$ excite mostly spin-up (majority band) electrons from the $2p_{3/2}$ level and since the empty states available at the fermi level are mostly spin-up, the absorption is enhanced relative to the unpolarised spectrum. The same photons excite mostly spin-down electrons from the $2p_{1/2}$ level so the absorption is reduced relative to the unpolarised spectrum. The opposite is true for the negative helicity μ^- photons ($\boldsymbol{L} = -1$). Reproduced from [4]

example spectra are from a sample containing Fe. The difference in the spectra between the parallel and antiparallel alignments of $\boldsymbol{L}$ and $\boldsymbol{M}$, that is, the dichroism, is clear and the dichroic spectrum can be analysed to determine the orbital and spin magnetic moments of the atoms.

The fundamental mechanism that produces the $L_{2,3}$-edge dichroism is normally described as a two-step process [3] illustrated in Fig. 10.2 [4]. In the first step, circularly polarised photons excite spin-polarised electrons from the spin–orbit split $2p$ level. In the case of positive helicity ($\boldsymbol{L} = +1$, electrons excited from the $2p_{3/2}$ level are 62.5% spin-up while those from the $2p_{1/2}$ level are 25% spin-up. The corresponding proportions for negative helicity ($\boldsymbol{L} = -1$) are 37.5% and 75%, respectively. These spin-polarised electrons are excited into the valence band and if this is spin-polarised then it acts as a spin filter for the polarised emission from the $2p$ level (step 2). Thus, in the case of a magnetised sample, the $L_{2,3}$ absorption spectrum shows a different spectral dependence for parallel and antiparallel alignments of $\boldsymbol{L}$ and $\boldsymbol{M}$.

As illustrated in Fig. 10.3 for Fe, Co, and Ni, the $L_{2,3}$ edges of the transition metals are at different X-ray energies [5]. The dichroism at each edge can be measured and thus the magnetic moments of the atoms of each element can be determined independently, which is especially important for samples containing more than one magnetic element.

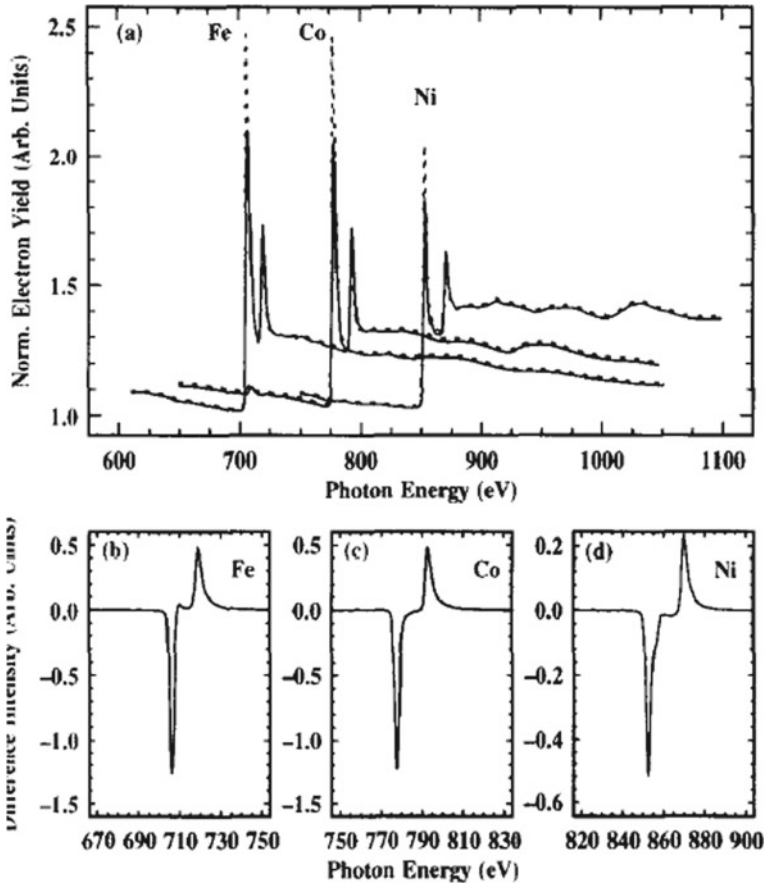

Fig. 10.3 XAS spectra and dichroism of the $L_{2,3}$ edges in thin films of Fe, Co, and Ni measured in transmission (Fig. 10.1a). Reproduced from [5]

The development of XMCD as a precise measuring tool of atomic magnetic moments began with the formulation of the sum rules for the absorption of circularly polarised X-rays by magnetic materials [6, 7]. The most important sum rules relate the projection of the spin $\langle S_Z \rangle$ and orbital $\langle L_Z \rangle$ magnetic moments along the photon polarisation direction to partial differential absorption cross sections at the L_2 and L_3 edges. Originally, these were derived using a graphical angular momentum technique [6, 7] but later, the same sum rules were obtained within a Fermi golden rule formalism [8, 9]. For transitions from core states with an angular momentum quantum number l_c to valence states with an angular momentum quantum number l_v, the orbital moment sum rule is given by [6]:

$$\langle L_z \rangle = 2\frac{l_v(l_v+1)}{l_c(l_c+1)-l_v(l_v+1)-2}\frac{\int_{\text{edge}}\left(\mu_{\uparrow\uparrow}(\omega)-\mu_{\uparrow\downarrow}(\omega)\right)\mathrm{d}\omega}{\int_{\text{edge}}\left(\mu_{\uparrow\uparrow}(\omega)+\mu_{\uparrow\downarrow}(\omega)+\mu_0\right)\mathrm{d}\omega}n_{\text{h}} \quad (10.1)$$

Here, $\mu_{\uparrow\uparrow}(\omega)$ and $\mu_{\uparrow\downarrow}(\omega)$ are the X-ray absorption spectra measured with the photon angular momentum parallel and antiparallel with the applied (saturating) magnetic field, respectively, and $\mu_0(\omega)$ is the average of the two, or, alternatively, the absorption spectrum measured with linearly polarised light. The term n_{h} is the number of holes per atom at the Fermi level, which for a solid state system, will be a non-integer number. For example, in the case of Fe, this is normally taken to be 3.39 holes per atom [10].

The integrals in this case are over the entire absorption edge. For absorption by a transition metal L edge, i.e. $2p$–$3d$ transitions, $l_c = 1$ and $l_v, = 2$ and using

$$\mu_0(\omega) = \frac{1}{2}\left(\mu_{\uparrow\uparrow}(\omega)+\mu_{\uparrow\downarrow}(\omega)\right) \quad (10.2)$$

(8.1) becomes:

$$L_z = \frac{4}{3}\frac{\int_{L_2+L_s}\left(\mu_{\uparrow\uparrow}(\omega)-\mu_{\uparrow\downarrow}(\omega)\right)\mathrm{d}\omega}{\int_{L_2+L_s}\left(\mu_{\uparrow\uparrow}(\omega)+\mu_{\uparrow\downarrow}(\omega)\right)\mathrm{d}\omega}n_{\text{h}} \quad (10.3)$$

Thus, the orbital moment is proportional to the total area in the dichroism spectrum.

The projection of the spin moment along the photon spin is given by [7]:

$$\begin{aligned}&\frac{l_v(l_v+1)-2-l_c(l_c+1)}{3l_c}S_z\\&+\frac{l_v(l_v+1)[l_v(l_v+1)+2l_c(l_c+1)+4]-3(l_c-1)^2(l_c+2)^2}{6l_vl_c(l_v+1)}T_z\\&=\frac{\int_{j^+}\left(\mu_{\uparrow\uparrow}(\omega)-\mu_{\uparrow\downarrow}(\omega)\right)\mathrm{d}\omega-\left(\frac{l_c+1}{l_c}\right)\int_{j^-}\left(\mu_{\uparrow\uparrow}(\omega)-\mu_{\uparrow\downarrow}(\omega)\right)\mathrm{d}\omega}{\int_{\text{edge}}\left(\mu_{\uparrow\uparrow}(\omega)+\mu_{\uparrow\downarrow}(\omega)+\mu_0\right)\mathrm{d}\omega}n_{\text{h}}\end{aligned} \quad (10.4)$$

where $< T_Z >$ is the expectation value of the magnetic dipole operator along the photon spin and is a measure of the anisotropy of the spin distribution, which XMCD is sensitive to since the photon polarisation samples a directional cut through the atomic electron density. This term, discussed in more detail below, is small relative to $<S_Z>$ and for bulk samples has often been assumed to be zero but its significance increases in nanoscale particles and it must be taken into consideration. Note that the integrals in the numerator of (4) are taken over individual j components of the L edge.

In the case of transition metal L edges (4) becomes.

$$\langle S_z \rangle + \frac{7}{2} T_z = \frac{\int_{L_s} \left(\mu_{\uparrow\uparrow}(\omega) - \mu_{\uparrow\downarrow}(\omega)\right) \mathrm{d}\omega - 2 \int_{L_2} \left(\mu_{\uparrow\uparrow}(\omega) - \mu_{\uparrow\downarrow}(\omega)\right) \mathrm{d}\omega}{\int_{L_2+L_s} \left(\mu_{\uparrow\uparrow}(\omega) + \mu_{\uparrow\downarrow}(\omega)\right) \mathrm{d}\omega} n_h \tag{10.5}$$

Figure 10.4 shows simulated dichroic XAS with a fitted integral background. Figure 4b, c shows the background-subtracted μ_0 signal and the dichroism. The relevant integrals appearing in the $<L_Z>$ and $<S_Z>$ sum rules are also indicated on

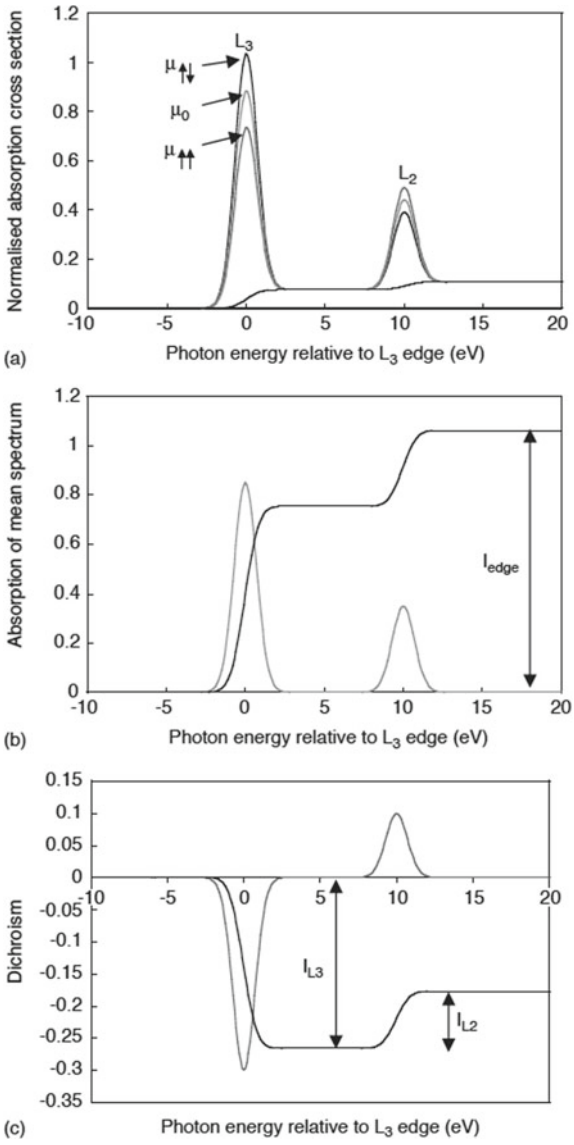

Fig. 10.4 XAS Simulated XAS and dichroism spectra for a transition metal *L* edge showing the relevant integrals used in the sum rules. Reproduced from [11]

the figure and labelled:

$$I_{\text{edge}} = \frac{1}{2} \int_{L_2+L_s} \left(\mu_{\uparrow\uparrow}(\omega) + \mu_{\uparrow\downarrow}(\omega)\right) \mathrm{d}\omega \tag{10.6}$$

$$I_{L3} = \int_{L_s} \left(\mu_{\uparrow\uparrow}(\omega) - \mu_{\uparrow\downarrow}(\omega)\right) \mathrm{d}\omega \tag{10.7}$$

$$I_{L2} = \int_{L_2} \left(\mu_{\uparrow\uparrow}(\omega) - \mu_{\uparrow\downarrow}(\omega)\right) \mathrm{d}\omega \tag{10.8}$$

In the simplest analysis for 3d transition metals, ignoring the $< T_Z >$ term, the spin and orbital sum rules reduce to:

$$\langle S_z \rangle = \frac{I_{L3} - 2I_{L2}}{I_{\text{edge}}} n_{\text{h}} \tag{10.9}$$

and

$$\langle L_z \rangle = \frac{4}{3} \frac{I_{L2} + I_{L3}}{I_{\text{edge}}} n_{\text{h}} \tag{10.10}$$

Since the quantities are normalised by the total edge absorption and given in terms of the number of valence band holes per atom, the values returned are the orbital and spin moments per atom.

The neglect of the $< T_Z >$ term is not valid in low-dimensional systems such as ultra-thin films since the high proportion of surface atoms introduces a significant anisotropy in the spin distribution and the spin term evaluated using (10.9) becomes measurably dependent on the angle of the sample normal with respect to the photon incidence direction. (Note that we assume throughout that the photon direction and sample magnetisation are parallel or antiparallel). It has been demonstrated that in the case of Fe nanoparticles, the dipole moment contribution increases as the particle size decreases [11].

Bruno has shown that the contribution of $< T_Z >$ to the measured spin moment with the sample normal at an angle θ with the photon beam varies as $\sin^2\theta$ [12]. If one can assume that the sample has rotational symmetry parallel to the substrate surface (the normal situation), then it can be shown [11] that the dipole moment goes to zero when $\tan^2 \theta = 2$, i.e. $\theta = 54.7°$, the so-called 'magic angle'. Thus, a measurement at the magic angle will yield the pure spin moment without the dipole contribution and is the value to be compared with other measurement techniques, for example, magnetometry (after including the orbital moment). Thus, the simple expedient of rotating the sample to an incidence angle of 55° relative to the photon

beam while maintaining the parallel and antiparallel alignment of the photon polarisation and sample magnetisation will eliminate the $<T_Z>$ term and (10.9) can be used to determine the spin moment.

10.2 Example System: Fe@Cr Core–Shell Nanoparticles

As pointed out earlier, XMCD is particularly powerful when investigating samples containing more than one element as it is able to chemically focus on the magnetic orbital and spin moments in individual elements. Whereas conventional magnetometry measures the average magnetic behaviour of all the elements in the sample. In recent years, the magnetic behaviour of ferromagnetic/antiferromagnetic interfaces has received particular attention due to the appearance of exchange bias after field-cooling, that is, a shift of the hysteresis loop of the magnetic material along the applied field axis [13, 14]. The effect is due to the 'pinning' of magnetic moments of the ferromagnetic material by exchange coupling with moments on the antiferromagnetic material at the interface and exchange bias is accompanied by an increase in coercivity. The effect is not only of interest from a fundamental perspective but is exploited in spin valves used for magnetic recording [15]. The majority of the work has focused on thin film interfaces but more recently an investigation using XMCD and magnetometry of the magnetic behaviour of Fe nanoparticles coated with one or two layers of Cr was reported [16].

The core–shell Fe@Cr nanoparticles were synthesised in ultra-high vacuum (UHV) in the gas-phase and matrix isolated in Ag films as illustrated in Fig. 10.5. The substrates used were C-coated Cu TEM grids and the finished samples had an X-ray transmission at the Fe L-edge in the range 10–90% and could be used for direct absorption measurements as illustrated in Fig. 10.1a. Three types of nanoparticles were prepared, that is, uncoated Fe nanoparticles, Fe cores with a single atomic layer of Cr, and Fe cores with two atomic layers of Cr (see Fig. 10.5c) thus the evolution of the magnetic behaviour as a function of the shell thickness could be studied.

The details of the analysis of the XMCD data is illustrated for the case of pure Fe nanoparticles in Fig. 10.6. The raw absorption data in transmission is shown in Fig. 10.6a and the same data after subtracting an integral background is plotted in Fig. 10.6b. The final dichroism spectrum after subtraction of a weak Ag N-edge absorption at 730 eV within the Fe $L_{2,3}$ absorption spectrum is shown in Fig. 10.6c. This is in a suitable form for sum rule analysis as illustrated in Fig. 10.4. In addition to obtaining the full XMCD spectrum, it is possible to obtain a magnetisation loop for a given element in the sample by simply measuring the intensity of the L_3 absorption edge as a function of the applied magnetic field intensity. The resulting curve is on a background signal that can easily be removed to produce loops such as that shown in Fig. 10.6d for pure Fe nanoparticles at a temperature of 204 K. The red line is a Langevin function at the same temperature that shows an optimum fit to the measured curve for a particle size of 2.68 nm (850 atoms). The inset in Fig. 10.6d compares the magnetisation measured by XMCD (black line) with that measured

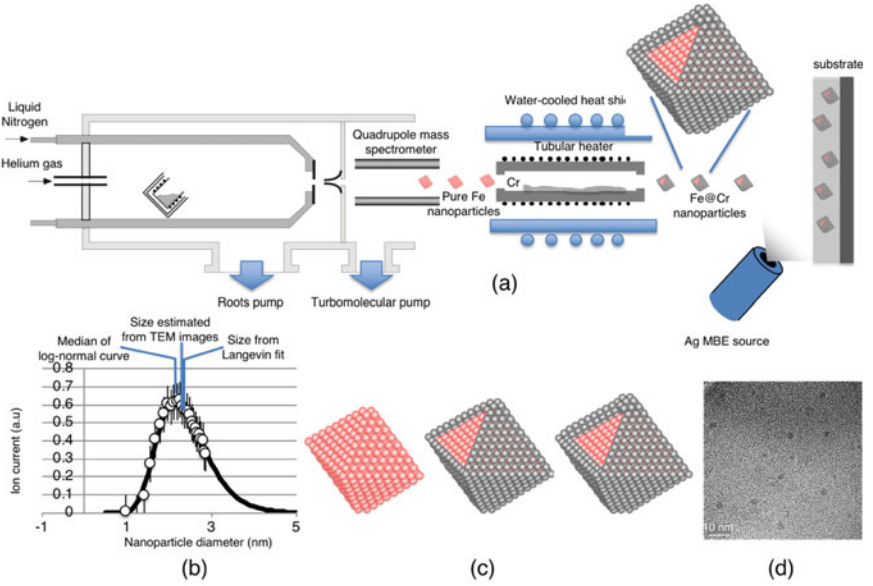

Fig. 10.5 **a** Synthesis of core−shell nanoparticles and production of matrix-isolated assemblies for XMCD and magnetometry studies. **b** Mass spectrum of pure Fe nanoparticles measured in the gas phase (open circles) fitted to a log−normal distribution (line). The spectrum is compared to the size determined by fitting Langevin functions to the magnetisation curves and estimated from TEM images. All three methods agree on the core particle diameter within the experimental uncertainty. **c** Illustration of the three types of nanoparticle studied, i.e. pure Fe, Fe@Cr with a monolayer shell, and Fe@Cr with a bilayer shell. **d** TEM image showing size distribution of Fe@Cr bilayer nanoparticles. Reproduced from [16]

from the same sample by a SQUID magnetometer (red line) demonstrating excellent agreement between the two methods.

The background subtracted XMCD spectra for pure Fe nanoparticles, Fe@Cr monolayer and Fe@Cr bilayer samples are compared in Fig. 10.7a. Even without detailed analysis, it is clear that the dichroism is weaker in the particles with the Cr shells showing that the magnetic moment of the Fe cores is reduced by the interaction with the Cr shell. The analysis using the sum rules presented in the previous section reveals the spin and orbital moments of the Fe cores plotted in the inset of Fig. 10.7a and listed in Table 10.1.

The general result is that coating the Fe cores with Cr does not significantly affect the orbital moment while the spin moment is reduced by around 40%. Note that the total Fe moment in the uncoated nanoparticles appears to be slightly less than the bulk value but this is an experimental artefact. The data above were taken at 204 K, whereas at 2 K, at which a higher level of saturation is reached, gives a measured total moment of 2.18 μ_B/atom. In addition, the data was taken at normal incidence at which, as discussed in the previous section, gives a contribution from the dipole

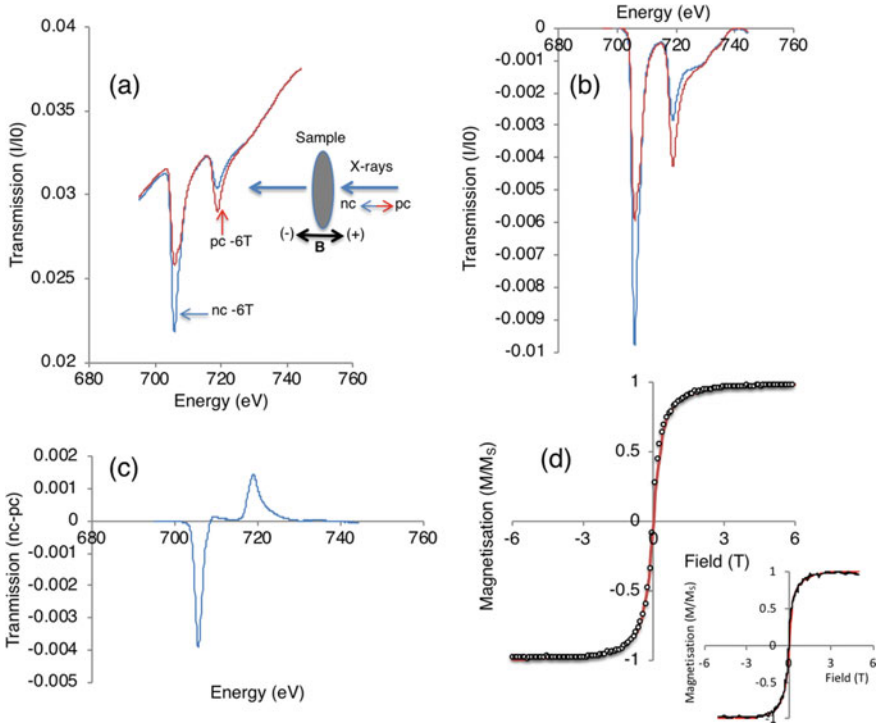

Fig. 10.6 **a** X-ray transmission in the Fe $L_{2,3}$ region of pure Fe nanoparticles in Ag with an applied field of − 6 T showing the difference in absorption between negative circular polarisation (nc) and positive circular polarisation (pc) of the X-rays. The inset shows the labeling of positive and negative directions of the applied field and photon angular momentum. **b** Absorption data after subtracting an integral background. **c** Fe $L_{2,3}$ dichroism used for sum rule analysis. **d** Sample magnetisation at 204 K (open circles) obtained by plotting the intensity of the Fe L_3 peak as a function of the applied field. The red line is a Langevin function plotted for a particle diameter of 2.68 nm. The inset compares the magnetisation measured by XMCD (black line) with that measured from the same sample by SQUID magnetometry (red line) showing excellent agreement. Reproduced from [16]

moment. Taking this into account gives a measured total Fe moment by XMCD of 2.28 μ_B/atom.

Whereas the low- temperature coercivity of the pure Fe nanoparticles and F@Cr monolayer particles is similar, there is a large increase observed in the Fe@Cr bilayer sample (Fig. 10.7b). In addition, field cooling the samples shows no indication of exchange bias on the pure Fe and F@Cr monolayer particles but a clear appearance of exchange bias in the Fe@Cr bilayer sample (Fig. 10.7c). The conclusion is that a shell thickness of at least two atomic layers of Cr around the Fe core is required to generate exchange bias and the accompanying increase in coercivity.

In an Fe nanoparticle containing 850 atoms, 40% of the atoms are at the surface so the XMCD data is suggestive that the layer of Fe atoms in contact with the Cr

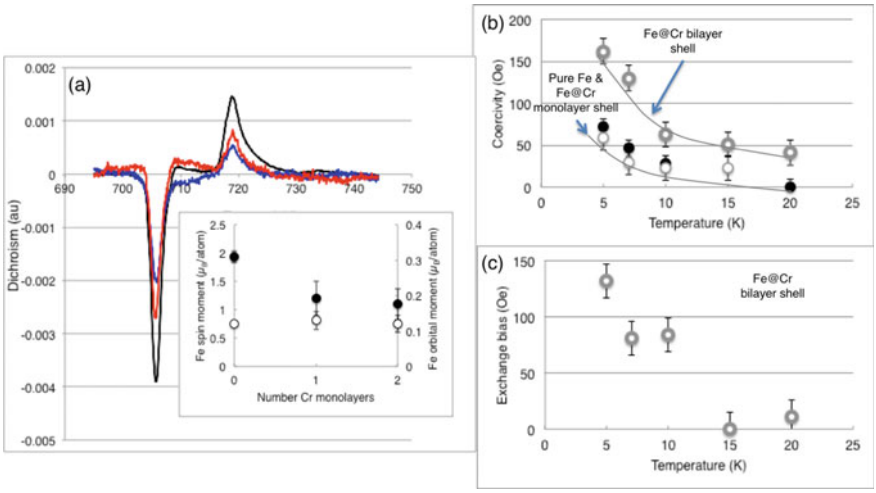

Fig. 10.7 **a** Normalised dichroism spectra (nc − pc, −6 T) for pure Fe (black line), Fe@Cr monolayer shell (red line), and Fe@Cr bilayer shell (blue line) nanoparticles in Ag matrices. The inset shows the variation of the Fe orbital (open circles) and spin (filled circles) magnetic moments with Cr shell thickness. **b** Coercivity after field cooling of pure Fe (filled circles), Fe@Cr monolayer shell (open circles with thin line), and Fe@Cr bilayer shell (open circles with thick line) nanoparticles in Ag matrices as a function of temperature. **c** Exchange bias of Fe@Cr bilayer shell nanoparticles in Ag matrices as a function of temperature after field cooling. Reproduced from [16]

Table 10.1 Fe orbital and spin moments bare Fe nanoparticles and for Fe nanoparticles coated with monolayer and bilayer Cr shells

Sample	Orbital moment/atom (μ_B)	Spin moment/atom (μ_B)	Total moment/atom (μ_B)
Fe nanoparticles	0.12 ± 0.02	1.83 ± 0.11	1.95 ± 0.11
Fe@Cr monolayer	0.13 ± 0.02	1.2 ± 0.3	1.3 ± 0.3
Fe@Cr bilayer	0.12 ± 0.02	1.1 ± 0.3	1.2 ± 0.3

shell is either magnetically disordered or antiferromagnetic. The conclusion of the work is that in the case of the monolayer shell, the interface is disordered while with the bilayer shell, some antiferromagnetic coupling is present. The level of exchange bias observed would require only a few Fe atoms to be pinned at the interface.

10.3 Future Perspectives

The emergence of the sum rules in the early 1990s was coincidental with an expansion in the number of third-generation synchrotron radiation sources, which use insertion devices to generate very high intensities of X-rays with variable polarisation. For a review of the development of the technique, see ref [17]. This led to a proliferation of XMCD experiments and initially the focus was on static thin films and nanostructures containing transition metals. The sum rules are equally applicable to rare-earth systems though a more complex analysis is required to extract the magnetic moments [18] and the field has matured and embraced complex rare-earth systems. These including magnetically doped topological insulators, important for spintronics applications [18] and DyFe/YFe exchange spring materials [4] that demonstrate giant magnetoresistance (GMR). The method has also evolved to include measurements with spatial and temporal resolutions and these developments are briefly illustrated with some examples in this section.

10.3.1 Spatially Resolved XMCD: Domain Imaging in Patterned Structures

XMCD can be combined with X-ray photoelectron microscopy (XPEEM) to provide spatially resolved images of magnetisation in samples. The principle of X-PEEM is illustrated in Fig. 10.8a and it consists of electron lenses that provide a magnified image of the sample at the image plane at which there is a two-dimensional detector. The secondary electrons are excited by a soft X-ray beam and as illustrated in Fig. 10.1b, if the photons are tuned to an element absorption edge, there will be a peak in the secondary electron yield at positions where that element is present, providing chemical mapping of a surface. If, in addition, the photon beam is circularly polarised, magnetic contrast at each position can be obtained by taking an image on and off the edge. This will reveal which regions have their magnetisation aligned with the photon spin (negative contrast) and which have their magnetisation aligned antiparallel to the photon spin (positive contrast). The direction of magnetisation sampled can be controlled by changing the angle of incidence of the photon beam. One of the major advantages of XMCD-XPEEM is that it combines magnetic imaging with chemical sensitivity.

Figure 10.8b–d shows domain patterns in micro-patterned Co rectangles with a thickness of 20 nm and aspect ratios of 1:1, 1:2, and 1:3. The Co squares show predominantly a vortex state domain structure, while the others show a variety of domain structures including symmetric and asymmetric vortex and antivortex states.

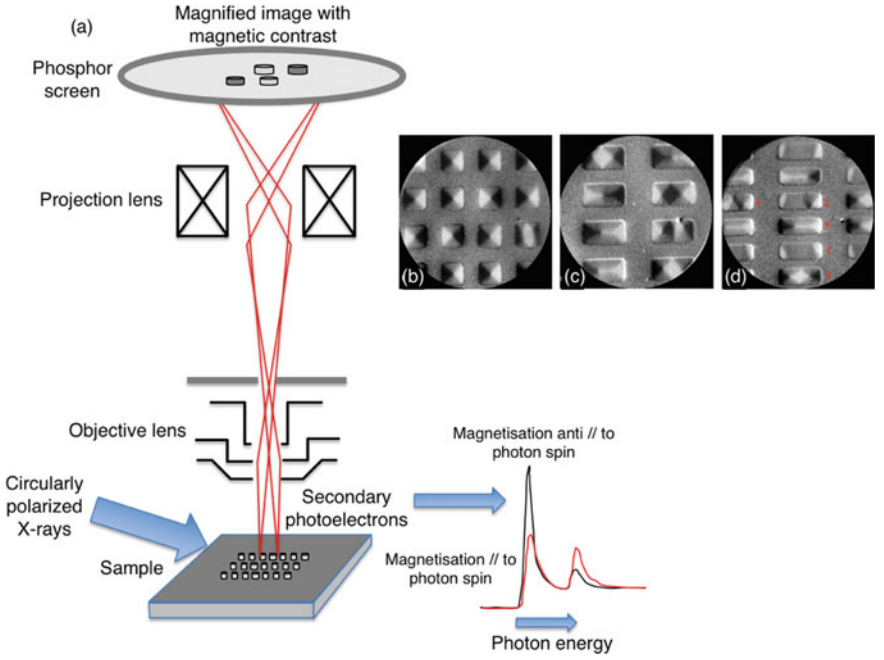

Fig. 10.8 **a** Schematic diagram of XPEEM combined with XMCD to produce surface magnetic imaging of a sample. **b–d** Magnetisation patterns in 20 nm thick Co rectangles with aspect ratios of 1:1, 1:2, and 1:3, respectively, with the photon beam from the left. Image size is 5 μm. Reproduced from [19]

10.3.2 Time-Resolved XMCD Measurements in Exchange-Coupled Layers

Synchrotrons that are mainly used for XMCD measurements are pulsed X-ray sources with a well-defined time structure. Thus, time-resolved magnetic measurements can be obtained by sampling the dichroism at a specific time from an X-ray pulse and this can be done simply by measuring the absorption intensity at an absorption edge for a fixed helicity of the X-rays. This will give the variation of magnetisation superimposed on a static background. A clock signal synchronous with the X-ray pulses can be used to drive a sample excitation, for example, a pulsed RF field that sets up ferromagnetic resonance (FMR) in a magnetic sample. Thus varying the time delay between the magnetisation pulse and the probing X-ray pulse enables a stroboscopic pump-probe measurement that measures the magnetisation state at a specific time following the excitation. The technique is referred to as X-ray-detected ferromagnetic resonance or XFMR [20]. A good demonstration of the technique has been published recently [21]investigating ferromagnetic resonance in exchange-coupled NiFe/CoNi bilayers (Fig. 10.9d). By measuring the dichroism at the Ni and

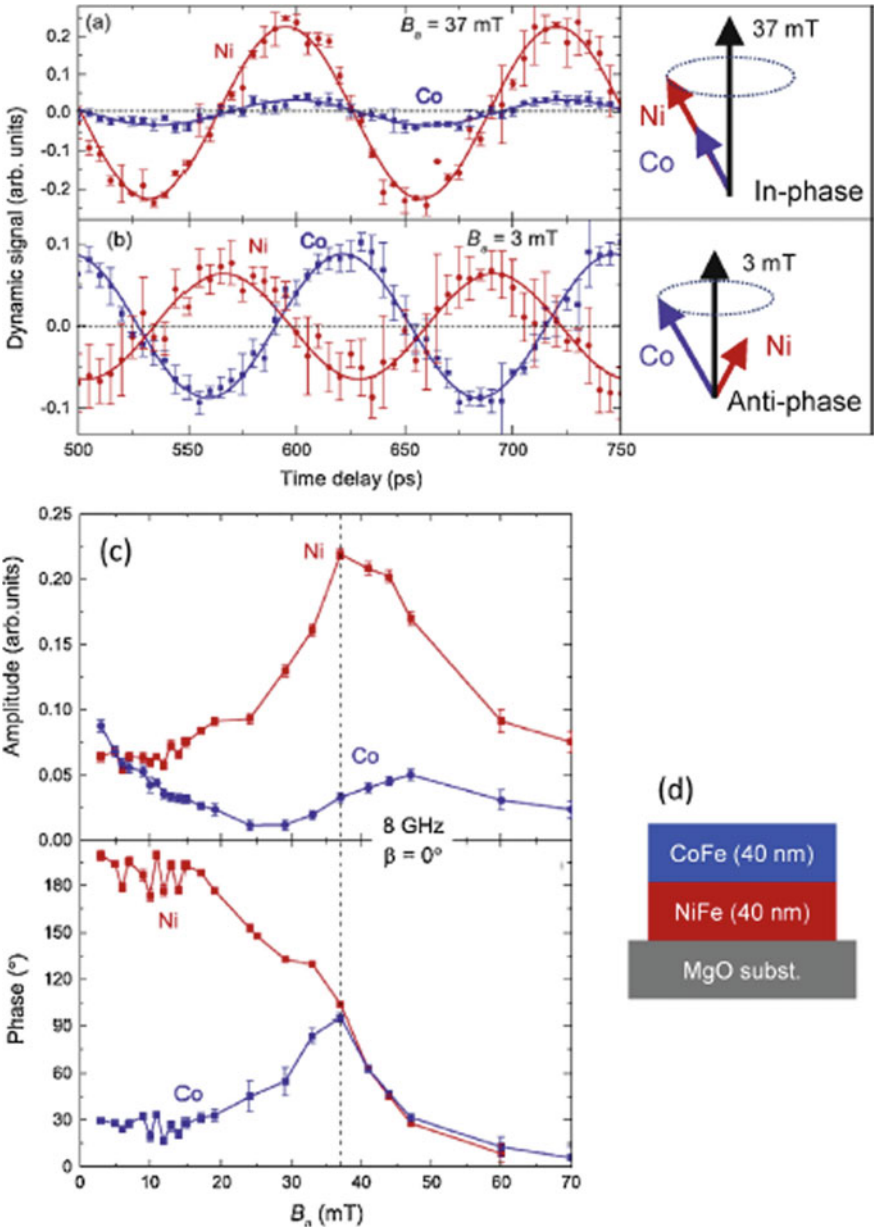

Fig. 10.9 XFMR results of exchange-coupled NiFe/CoFe bilayer. **a** and **b** XMCD signals measured at Co and Ni L_2 edges as a function of delay time between X-ray pulse and 8 GHz RF field. **a** and **b** show delay scans for the acoustic mode (at 37 mT) and optic mode (at 3 mT), respectively. The Co and Ni precession are anti-phase (167∘52) in the optic mode and in-phase (7∘52) in the acoustic mode. **c** XFMR precessional plots as a function of applied field showing the change in amplitude and phase of the Ni and Co precessions. **d** Schematics of the bilayer grown on MgO substrate. Reproduced from [20]

Co L-edge, it is possible to independently probe the dynamic behaviour in each section of the bilayer.

FMR measurements show two resonance states in the bilayer with applied static fields of 3 and 37 mT labelled the optic mode and the acoustic mode, respectively. In the acoustic mode, the magnetisation of both layers precesses in phase. The amplitude is strongest in the NiFe layer, and decays as it penetrates into the CoFe layer. In contrast, in the optic mode, magnetisations of the two layers precess in anti-phase and the amplitude is greatest in the CoFe layer. XFMR data was measured at the Ni and Co L_2 edges using circularly polarised X-rays with fixed helicity. The magnetic excitation pulse was at 8 GHz (125 ps period) and Fig. 10.9a, b shows the delay scans for the acoustic mode (at 37 mT) and optic mode (at 3 mT), respectively. In the acoustic mode, the Co and Ni spins precess in phase while in the optic mode, they are in anti-phase. The relative amplitudes confirm that the acoustic mode is mainly driven by the Ni layer and the optic mode is mainly driven by the Co layer.

The amplitude and phase of the Co and Ni signals are plotted in Fig. 10.3c and shows the behaviour expected of coupled driven oscillators.

References

1. J.L. Erskine, E.A. Stern, Phys. Rev. B **12**, 5016 (1975)
2. G. Schütz, W. Wagner, W. Wilhelm, P. Kienle, R. Zeller, R. Frahm, G. Materlik, Phys. Rev. Lett. **58**, 737 (1987)
3. J. Stöhr and Y. Wu, New directions in research with third generation synchrotron radiation sources, in *NATO ASI Series E: Applied Sciences*, eds. by A.S. Schlachter, F.J. Wuilleumier (Kluwer 1994), p. 221
4. G. Van der Laan, A.I. Figueroa, Co-ord. Chem Rev. **277–278**, 95 (2014)
5. J. Stöhr, J. Electr. Spectr. Re. Phenom. **75**, 253 (1995)
6. B.T. Thole, P. Carra, F. Sette, G Laan van der, Phys. Rev. B **68**, 1943 (1992)
7. P. Carra, B.T. Thole, M. Altarelli, X. Wang, Phys. Rev. Lett. **70**, 694 (1993)
8. M. Altarelli, Phys. Rev. B **47**, 597 (1993)
9. A. Ankudinov, J.J. Rehr, Phys. Rev. B **51**, 1282 (1995)
10. C.T. Chen, Y.U. Idzerda, H.-J. Lin, N.V. Smith, G. Meigs, E. Chaban, G.H. Ho, E. Pelligrin, F. Sette, Phys. Rev. Lett. **75**, 152–155 (1995)
11. C. Binns and J. Blackman, Chapter 9, section 9.2.6, in *Metallic Nanoparticles,* ed. by. J. Blackman (Elsevier, 2009). ISBN: 978-0-444-51240-6
12. P. Bruno, Phys. Rev. B **39**, 865 (1989)
13. J. Nogués, I.K.J. Schuller, J. Magn. Magn. Mater. **192**, 203–232 (1999)
14. A.E. Berkowitz, K.J. Takano, J. Magn. Magn. Mater. **200**, 552–570 (1999)
15. B. Dieny, V.S. Speriosu, S.S.P. Parkin, B.A. Gurney, D.R. Wilhoit, D. Mauri, Phys. Rev. B **43**, 1297–1300 (1991)
16. C. Binns, M.T. Qureshi, D. Peddis, S.H. Baker, P.B. Howes, A. Boatwright, S.A. Cavill, S.S. Dhesi, L. Lari, R. Kröger, S. Langridge, Nanoletters **13**, 3334–3339 (2013)
17. T. Funk, A. Deb, S.J. George, H. Wang, S.P. Cramer, Co-ord. Chem. Rev. **249**, 3–30 (2005)
18. A.I. Figueroa, A.A. Baker, S.E. Harrison, K. Kummer, G. van der Laan, T. Hesjedal, J. Magn. Magn. Mater. **422,** 93–99 (2017)
19. S. Cherifi, R. Hertel, J. Kirschner, H. Wang, R. Belkhou, A. Locatelli, S. Heun, A. Pavlocska, E. Bauer, J. Appl. Phys **98**, 043901 (2005)
20. G. van der Laan, J. Electr. Spectr. Rel. Phenom. **220**, 137–146 (2017)

21. G.B.G. Stenning, L.R. Shelford, S.A. Cavill, F. Hoffmann, M. Haertinger, T. Hesjedal, G. Woltersdorf, G.J. Bowden, S.A. Gregory, C.H. Back, P.A.J. de Groot, G. van der Laan, New J. Phys. **17**, 013019 (2015)